

Selectively Exciting and Probing Radiative Plasmon Modes on Short Gold Nanorods by Scanning Tunneling Microscope-Induced Light Emission

Yalan Ma,* Olivier J. F. Martin, and Andreas Stemmer*



Cite This: *ACS Photonics* 2023, 10, 743–750



Read Online

ACCESS |

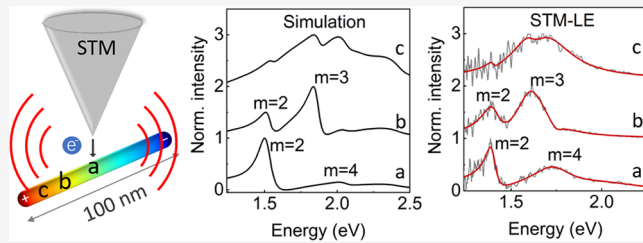
Metrics & More

Article Recommendations

Supporting Information

ABSTRACT: We study the plasmon modes of gold nanorods (as short as ~ 100 nm) on a nonmetallic conductive substrate using scanning tunneling microscope-induced light emission (STM-LE) with a nonplasmonic tungsten tip at room temperature in high vacuum (10^{-7} mbar). The far-field light is identified as the radiative decay of plasmon modes on the nanorods excited by inelastic electron tunneling. The spatial intensity distributions of the first three longitudinal multipolar modes on nanorods are spatially resolved on the order of 10–20 nm. These intensity distributions are related to the radiative electromagnetic local density of states and agree very well with numerical simulations. We discover that the presence of the tungsten tip with a high-dielectric constant influences the line shapes of the plasmon spectra and enhances the strength of the plasmon peaks.

KEYWORDS: Au nanorods, plasmons, scanning tunneling microscope, light emission, inelastic electron tunneling



INTRODUCTION

Plasmonic nanoantennas are key nano-optics components, thanks to their tunable electromagnetic local density of states (EM-LDOS).¹ As an analogy to the electronic density of states in semiconductors, the EM-LDOS is defined as the density of electromagnetic (EM) modes per energy unit in real space. The EM-LDOS also describes the plasmon modes' density that can be supported by a plasmonic nanoantenna.^{2,3} By tuning the EM-LDOS to the corresponding spectral range, one can enhance the efficiency of photovoltaic devices^{4,5} and photodetectors,^{6,7} as well as increase the spontaneous emission rate of quantum emitters.⁸ Furthermore, in optical spectroscopy, plasmonic nanoantennas enhance the light–matter coupling through strongly localized EM fields.^{9,10}

The characterization of the EM-LDOS (i.e., of the plasmon modes) is essential in nanoantenna design and different techniques have been developed to probe the EM-LDOS, such as optical microscopy^{11–14} and electron microscopy.^{15–23} For optical methods, the excitation of plasmon modes is restricted by the polarization of light,^{12,13} and the spatial resolution is limited by the diffraction of light or the sizes of near-field probes. For electron microscopy, for instance, electron energy loss spectroscopy (EELS)^{15–19} and cathodoluminescence (CL),^{15,17–23} the electron beam works as a broad-band point dipolar source oscillating above the sample surface.^{17,22} The electron beam excites the plasmons on metallic nanostructures locally and provides enhanced spatial resolution. EELS spectra present the full (including both radiative and nonradiative) EM-LDOS projected along the orientation of the point dipole,

while CL spectra show the projected radiative EM-LDOS.¹⁷ The scanning tunneling microscope-induced light emission (STM-LE) is also known to probe the radiative EM-LDOS by measuring the far-field emission light from plasmons excited by inelastic electron tunneling (IET).^{24–28} Similar to electrons in EELS and CL, IET electrons can also be represented as a point dipole oscillating along the tunneling direction.²⁵ Both electron microscopy and STM-LE can spatially probe plasmons on a scale of 1 nm or slightly above.^{23,24,29} Compared with CL and EELS, STM-LE provides a low-voltage technique with higher excitation energy resolution and shorter interaction range to study the radiative EM-LDOS of plasmonic nanostructures, while at the same time image their surface topography. STM-LE setups operating in ultra-high vacuum (UHV) at cryogenic temperatures may achieve the highest resolution spatially and in energy (for a recent overview, see ref 30), albeit at the cost of much more cumbersome specimen exchange and positioning compared with electron microscopy.

In this work, we perform experimental measurements and numerical calculations on the far-field radiation of short Au nanorods by STM-LE. In previous publications, multipolar

Received: December 6, 2022

Published: February 23, 2023



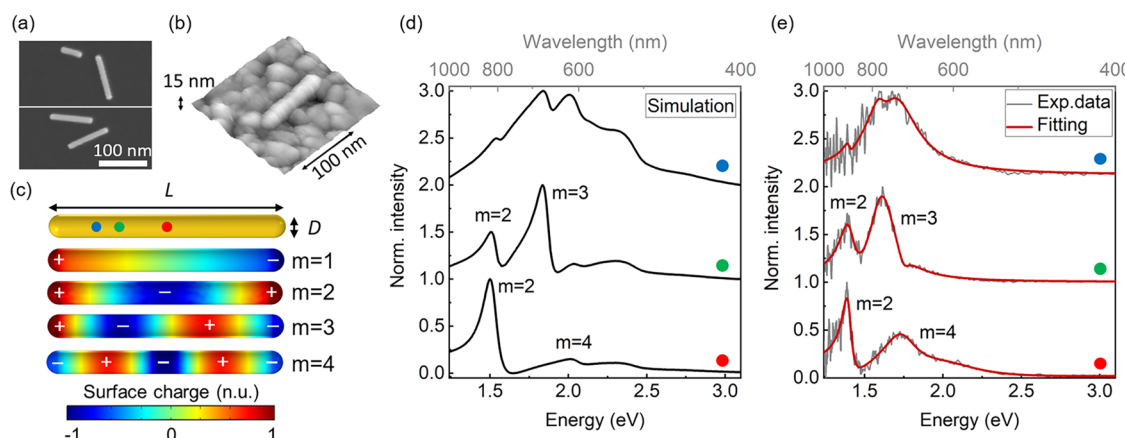


Figure 1. (a) SEM images of Au nanorods on a Si substrate. (b) STM topography image of a single Au nanorod on an ITO substrate. The STM parameters are -1.5 V and 100 pA. (c, d) Simulation results for an Au nanorod with a length $L = 100$ nm and diameter $D = 10$ nm. (c) Surface charge distribution of the dipolar mode ($m = 1$) and multipolar modes ($m = 2, 3, 4$). The charges are normalized to the maximum and minimum of each mode. (d) Normalized emission spectra obtained at different excitation locations (marked in panel (c) with colored dots). (e) STM-LE spectra acquired at the same locations on a nanorod of apparent length 123 ± 2 nm and width 32 ± 2 nm (not corrected for tip convolution). Gray lines are normalized experimental data and red traces are fitting results. The STM-LE parameters are -3.5 V, 50 nA, and 60 s. The spectra in panels (d) and (e) are vertically shifted for legibility.

plasmon modes on metallic nanorods have been resolved spatially using EELS^{16,19} or CL.^{17,20} Here, in our work, we use STM-LE to probe the radiative EM-LDOS of Au nanorods with a length as short as ~ 100 nm. Up to three longitudinal multipolar plasmon modes on Au nanorods are excited by STM electrons. The spatial intensity distributions of different plasmon modes agree well with the radiative EM-LDOS in numerical simulations. Furthermore, these plasmon modes exhibit tip bias-dependent intensities, caused by the IET excitation mechanism.

Additionally, asymmetric line shapes due to Fano resonances³¹ are observed in both simulated and experimental STM-LE spectra. This asymmetry is induced by the surrounding dielectric environment, including the substrate and the STM tip. Moving the position of the STM tip changes the overall dielectric environment, resulting in small wavelength shifts for the plasmon modes. Furthermore, the plasmon wavelengths depend linearly on the aspect ratio of the nanorods for each multipolar mode. This agrees with theoretical calculations³² and experimental observations in optical spectroscopy.¹⁴

RESULTS AND DISCUSSION

We conduct both numerical calculations and STM-LE experiments to study the radiative plasmon modes of Au nanorods on an indium tin oxide (ITO) substrate. A tungsten tip is used to avoid exciting the tip–sample gap plasmons, thanks to the nonplasmonic optical behavior of tungsten in the measured spectral range.^{25,33} Figure 1a shows scanning electron microscopy (SEM) images of Au nanorods on a silicon substrate. The nanorods have identical diameters (D) of 11 ± 1 nm and lengths (L) that range from 55 to 155 nm, as determined by SEM. Figure 1b displays the STM topography of an Au nanorod on the rough ITO substrate. Figure 1c presents the simulation results for the surface charge distribution of different longitudinal plasmon modes on an Au nanorod with $L = 100$ nm and $D = 10$ nm. The surface charge distributions are characteristic of a dipolar mode ($m = 1$) and multipolar modes ($m = 2, 3$, and 4), which can also be understood in terms of standing wave-like Fabry–Pérot

resonances.^{13,32,34} The modes with $m = 2$ and 4 show symmetric charge distributions, and the modes with $m = 1$ and 3 show asymmetric charge distributions. For Fabry–Pérot cavity resonances, the two nanorod extremities work as reflecting mirrors and surface plasmons propagate back and forth along the nanorod.^{32,34} According to ref 32 two counter-propagating plasmon waves are excited in the nanorod, which can interfere and generate Fabry–Pérot resonances. Therefore, for each plasmon mode, the surface charge density shows standing wave-like features.

Figure 1d,e compares the simulated and experimental STM-LE spectra when the nanorod is excited at three different locations indicated as color dots in Figure 1c. When a voltage is applied to the STM tip, electrons can tunnel inelastically through the tip–sample junction and excite the plasmon modes on the Au nanorods. The excited plasmons decay radiatively and generate photons.²⁷ The probability of this IET process scales with the difference of tip bias voltage (V_{bias}) and plasmonic photon energy.^{35,36} Hence, the simulated spectra are corrected for the tip bias voltage used in experiments (additional details are provided in Methods). Different longitudinal plasmon modes are selectively excited depending on the location of the STM tip.^{26,37} The plasmon modes show spatial intensity variations, and further investigation will be presented later. We find that spectra obtained from simulations and experiments show asymmetric line shapes typical of Fano interference.^{13,31,38} The experimental STM-LE spectra can be very well fitted by the following Fano profiles¹⁴

$$I = C + \sum_m A_m \frac{(q_m \Gamma_m/2 + (E - E_m))^2}{(\Gamma_m/2)^2 + (E - E_m)^2} \quad (1)$$

Here, I is the spectral intensity and E is the photon energy. For mode m , E_m and Γ_m correspond to the resonance energy and the full width of the plasmon peak, q_m is the Fano parameter, and A_m and C are constant coefficients. Each plasmon mode is fitted with one Fano-line peak. The whole spectrum is a sum of all plasmon modes. In our experiments, only multipolar plasmon modes ($m > 1$) are detectable, since the longer

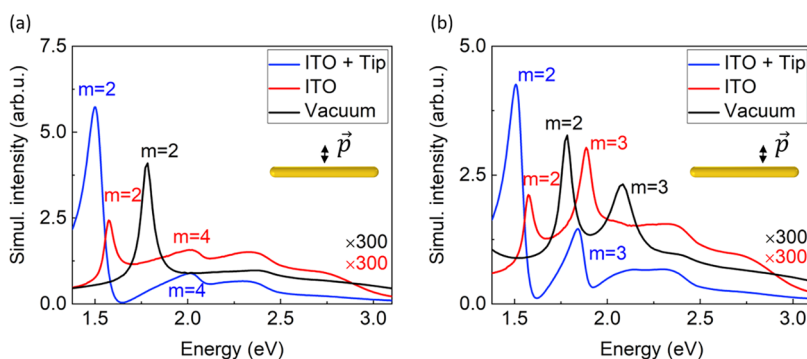


Figure 2. Simulated light emission intensity of an Au nanorod excited at the middle (a) and an off-center location (b) in three different dielectric environments: ITO substrate with a tungsten tip included, ITO substrate without the tip, and vacuum. Red and black curves are multiplied by a factor of 300.

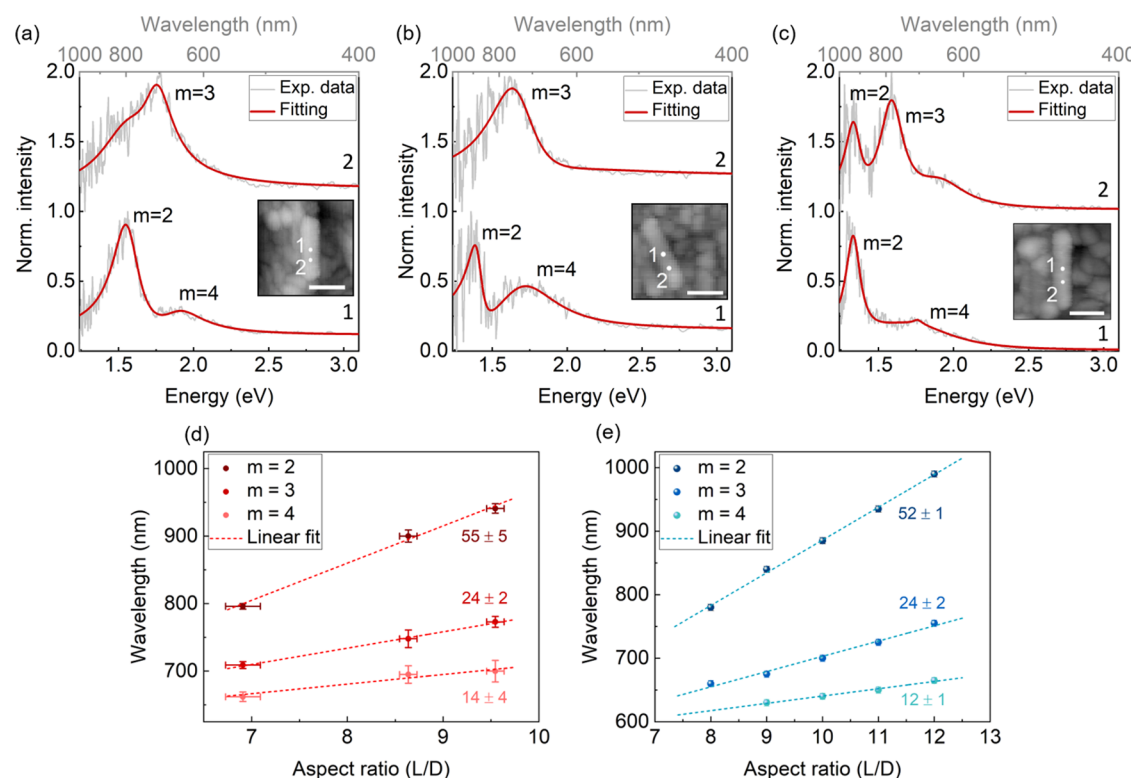


Figure 3. (a)–(c) STM-LE spectra measured at different locations on three different nanorods. Gray lines are normalized experimental data and red curves are fitting results using eq 1. The different plasmon modes are labeled with their mode numbers. The excitation positions of each spectrum are marked in the insets, which show the STM topography images of the nanorods (scale bar: 50 nm). The nanorods in panels (a)–(c) are measured to be 96 ± 2 nm, 115 ± 2 nm, and 125 ± 2 nm long, respectively. Their apparent widths are 32 ± 2 nm. The STM-LE parameters are -3.5 V, 40 nA, and 60 s. (d) and (e) Mode wavelength λ_m as a function of the aspect ratio of nanorods acquired from STM-LE and simulation, respectively. The data are fitted to linear curves.

wavelength dipolar mode ($m = 1$) is outside the sensitivity range of our spectrometer.

It has been reported that both the dielectric environment^{39,40} and the overlap of the interfering modes^{19,38} can give rise to Fano-like resonances. In the situation of mode interference, the spectral overlap of two different plasmon modes will have a constructive interference if they are in phase with each other. Conversely, two modes out of phase will have a destructive interference. These two interferences will lead to asymmetric line shapes. In the situation of a nonuniform dielectric environment, image charges generated in the dielectric environment interact with the charges in the nanorods, which also leads to a Fano resonance.

To elucidate the origin of the asymmetric line shapes and clarify the role of the substrate in our study, we explore different local dielectric environments as shown in Figure 2, where we consider both excitations at the middle and an off-center location. When the nanorod is in vacuum, the spectra exhibit the emission peaks of multipolar modes ($m = 2, 3$) with symmetric Lorentzian line shapes. When the Au nanorods are on an ITO surface, both modes are red-shifted due to the increased dielectric constant of the environment.^{41,42} Weak Fano asymmetries are also observable in this case. Furthermore, when the STM tip is applied, mode 2 gets further red-shifted and becomes more asymmetric with a steep slope appearing at the short wavelength side. Additionally, the

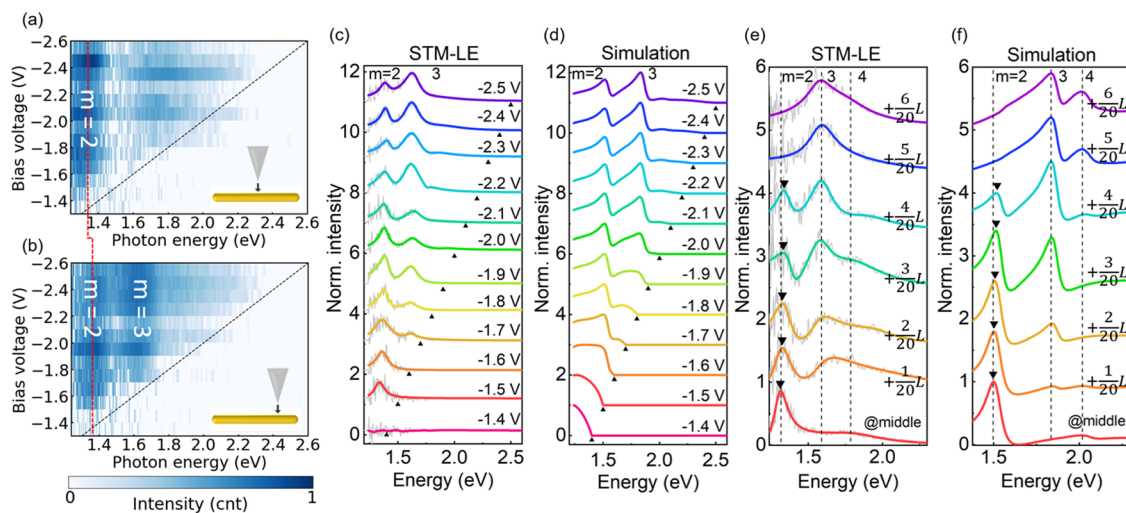


Figure 4. (a, b) STM-LE light intensity as a function of photon energy and bias voltage (V_{bias}) at two different locations (indicated in the insets) on the same nanorod with length 104 nm. The black dashed lines mark the quantum cutoff (eV_{bias} equals the photon energy). The red dashed lines indicate the peak position of mode 2. Normalized spectra from STM-LE (c) and simulation (d) as a function of tip bias. The quantum cutoff is marked by black triangles. The STM-LE parameters are 50 nA and 100 s. Normalized spectra from STM-LE (e) and simulation (f) at different offsets from the middle on the same nanorod. The bottom curves are acquired from the middle of the nanorod. The other spectra are acquired at locations with a distance increment of $\frac{1}{20}L$ for panels (e) and (f). Dashed lines mark the position of modes $m = 2, 3$, and 4. Triangles mark the peak maxima. STM-LE spectra are fitted with Fano profiles. The STM-LE parameters are -3.5 V, 40 nA, and 60 s.

presence of the tip enhances the local EM field and increases the strength of the plasmon modes (for more information refer to Figures S1 and S2). Thus, we conclude that the plasmon modes with Fano line shapes are caused by the high-dielectric environment, similar to the behavior of silver cubes on glass substrates³⁹ and Au nanorods on silicon substrates.⁴⁰

Next, we study the influence of nanorod length on STM-LE spectra. Figure 3a–c shows STM-LE spectra of three Au nanorods with different lengths acquired at different locations but with the same tip. We measure the following apparent lengths in Figure 3: 96 ± 2 nm in panel (a), 115 ± 2 nm in panel (b), and 125 ± 2 nm in panel (c), and we note that the STM images show an identical width (32 ± 2 nm) for all of the nanorods, indicating that the tip shape does not change during the measurements. Assuming isotropic tip shape and tip–sample convolution, the lengths can be estimated for the nanorods in Figure 3 as 75 ± 2 nm in panel (a), 94 ± 2 nm in panel (b), and 104 ± 2 nm in panel (c). The nanorod in Figure 3c exhibits red shifts of all of the modes compared with the short nanorod in Figure 3a. This agrees well with the model introduced by Douillard et al.,³² for the resonance wavelength λ_m of nanorods as a function of the mode order m and the nanorod dimensions (L, D)

$$\lambda_m = \frac{\lambda_p}{a_1} \left(\frac{1}{m} \frac{L}{D} + \frac{1}{m} + a_2 \right) \quad (2)$$

where λ_p is the plasma wavelength of gold and a_1 and a_2 are two coefficients, which depend on the dielectric constants of the nanorod and the environment.⁴³ Figure 3d,e summarizes the measurement and simulation results for the mode wavelengths λ_m for nanorods with different aspect ratios. We observe a linear dependence of the mode wavelengths on the aspect ratio, which agrees well with eq 2. Furthermore, a plasmon mode with higher order has a smaller slope in this linear fit, which is also in good agreement with eq 2. Compared with the simulations, the experimental STM-LE exhibits

slightly larger slopes and a red shift (65–80 nm) of each mode, which may be assigned to minor deviations in the geometry, e.g., tip dimension, substrate thickness, and nanorod diameter. Other possible explanations for the observed discrepancy include the underestimation of the dielectric constant of the environment,^{41,42} and a deviation in dielectric constant between Au nanorods and bulk Au⁴⁴ used in simulations. In any case, the agreement in Figure 3 between experimental and numerical data is very good.

In the following, we study the excitation mechanisms of the plasmon modes. In CL and STM-LE, the measured far-field light is generated from the radiative decay of the near-field plasmon modes excited by a broad-band electron source.^{25,36} Different from CL electrons, which are in an energy range of several kiloelectron volts, the energy of STM electrons can be finely tuned by the bias voltage to gain further insight into the excitation mechanisms of the plasmon modes. STM-LE spectra with different tip biases and a constant tunneling current are measured when placing the tip at the middle of the nanorod or 24 nm from the middle. Figure 4a,b shows the STM-LE intensity in the photon energy range of 1.3–2.6 eV with the tip voltages V_{bias} between -1.3 V and -2.5 V for a nanorod with length 104 nm. When $V_{\text{bias}} > -1.4$ V, no light is detected. When V_{bias} decreases, the first peak corresponding to the mode $m = 2$ is detected. When further decreasing V_{bias} , the second peak ($m = 4$ in Figure 4a and $m = 3$ in Figure 4b) emerges. As shown in Figure 4a,b, no light is detected with photon energy higher than ~ 2.3 eV. This agrees with eq 2, where λ_m is limited by the plasma frequency of gold when $m \rightarrow \infty$. For a tip bias from -1.8 to -2.1 V, overbias light emission is observed, where the energy of the emitted photon ($h\nu$) exceeds the quantum cutoff corresponding to the maximum electron energy (eV_{bias}). This overbias emission is frequently observed in STM-LE through multielectron⁴⁵ or nonlinear processes.⁴⁶ The origin of this phenomenon still needs further research.

Figure 4c plots normalized spectra with different V_{bias} from Figure 4b. When $V_{\text{bias}} = -1.4$ V, no light is detected in

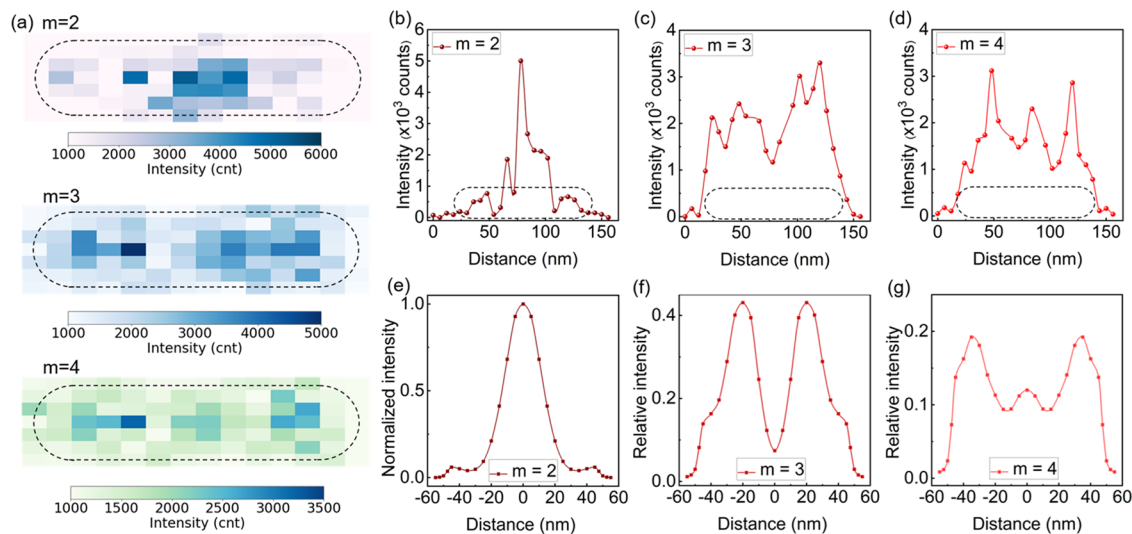


Figure 5. (a) Experimental STM-LE intensity maps for modes $m = 2, 3$, and 4 . The pixel size is $10 \times 5 \text{ nm}^2$. The black dashed lines denote the nanorod edge. (b)–(d) Experimental results for the light intensity of different plasmon modes versus distance along the nanorod long axes. The dashed lines mark the nanorod outline. The STM parameters are -3.5 V , 40 nA , and 60 s . The wavelengths of modes $m = 2, 3$, and 4 are $915.8, 766.0$, and 687.9 nm , respectively. (e)–(g) Same as panels (b)–(d) but obtained from simulations and shown with respect to the nanorod center to emphasize the symmetry of the intensity distribution. The nanorod has a length of 100 nm . The simulated intensity of mode 2 is normalized to its maximum, and the intensities of the higher modes are divided by the maximal intensity of mode 2.

experiments due to the limited sensitivity of our detector. When $-1.7 \text{ V} > V_{\text{bias}} > -2.1 \text{ V}$, mode 2 displays a higher intensity than mode 3. When $V_{\text{bias}} \leq -2.1 \text{ V}$, the intensity of mode 3 surpasses mode 2. This intensity variation can be explained by the IET process. The emission intensity of plasmons generated by IET is determined by the probability of IET electrons and the radiation efficiency. Because the probability of the IET process is proportional to the difference between eV_{bias} and the emitted photon energy, we multiplied the simulated spectra by a factor $(eV_{\text{bias}} - h\nu)$ for each trace.²⁵ In Figure 4d, the simulated intensity ratio between modes 2 and 3 shows an identical dependence on V_{bias} , whereas the intensity of mode 3 surpasses that of mode 2 when V_{bias} is between -2.1 and -2.2 V . In this simulation, the tip position is fixed for all tip bias voltages. This is because the tip–sample distance change is small in the measured tip bias range.

We now measure the dependence of the mode energy on the excitation location on the same nanorod. In Figure 4a,b, mode 2 shows a slight blue shift when moving the STM tip from the middle of the nanorod toward an end. To understand the change of the mode energy, STM-LE measurements and simulated spectra are acquired at different locations on the nanorod, as shown in Figure 4e,f. In both STM-LE measurements and simulations, mode 2 experiences a continuous blue shift, while modes 3 and 4 show no significant shift. To further study this phenomenon, we perform simulations on Au nanorods in two different situations: with an STM tip fixed at the middle of the nanorod and without an STM tip. As shown in Figure S3, no shift is observed for a fixed tip and without a tip. Thus, the shifting of mode 2 in Figure 4 can be attributed to the change in the dielectric environment surrounding the nanorod when moving the tip from one place to another.

Additionally, we investigate the spatial intensity distribution of plasmons. Figure 5a presents the STM-LE intensity for modes $m = 2, 3$, and 4 of the nanorod in Figure 1b. STM-LE spectra are acquired on a grid of $10 \text{ nm} \times 5 \text{ nm}$. To obtain the wavelengths of each plasmon mode, we first determine the

location with the highest plasmon peak. Then, the intensity at the corresponding wavelength is mapped along the entire nanorod. For each excited mode, the intensity spatial distribution shows a specific pattern.

For a higher accuracy, we perform line scans at the peak wavelength along the long axis of the nanorod. The results are shown in Figure 5b–d. For modes $m = 2, 3$, and 4 , the STM-LE shows 1, 2, and 3 intensity peaks along the nanorod axis, respectively. Similar results are obtained in the simulations as shown in Figure 5e–g. Furthermore, the intensity decreases with a higher mode number. This is due to the reduction of the radiative damping for higher-order modes and the increase of absorption losses in higher energy regimes.^{14,47} Additionally, the STM-LE intensity distributions along the long axis of the nanorod closely follow the radiative EM-LDOS profiles (see Figure S4), except for a small discrepancy at the two extremities. This discrepancy is due to the presence of the STM tip and the dielectric substrate.

CONCLUSIONS

Using STM-LE and nonplasmonic tips, we studied the optical properties of short Au nanorods deposited on nonmetallic ITO substrates and compared the measurements with numerical simulations. Due to the nonplasmonic properties of the tip and substrate, no tip–sample cavity plasmons are excited. The light emission collected in the far-field originates from the radiative decay of different longitudinal plasmon modes excited by IET electrons. In particular, the spatial intensity distribution of the first three multipolar modes for Au nanorods is measured on a lateral scale of $10–20 \text{ nm}$. The plasmonic peak intensity depends on the applied tip bias voltage and the photon energy, as expected for excitation by the IET process. The good match between measured and simulated spectra enables us to establish a link between STM-LE and the radiative EM-LDOS of Au nanorods. Thus, our approach provides the ability to probe the optical properties of the plasmonic nanostructures and characterize the spatial distribution of optical modes at the

nanometer scale. STM-LE appears promising for the development of optoelectronic devices that rely on plasmonic nanoantennas.^{48,49} Understanding IET-driven devices provides strategies to control the emission spectrum and efficiency.

METHODS

Sample Preparation. The samples are prepared with the drop-casting method.⁵⁰ Au nanorod colloid solution is purchased from Nanopartz (product number: A12–10–1400-CTABDIH-1-5). The substrates are glass slides with a 120–160 nm thick indium tin oxide (ITO) layer (Sigma-Aldrich, CAS: 50926-11-9). The nanorod concentration is first increased by a factor of 10 by centrifugation to obtain a good distribution on the ITO surface. Then, a drop of the nanorod solution is deposited on the ITO surface. After drying, the sample is rinsed with de-ionized water. The residual capping molecules around nanorods are removed by oxygen plasma (PVA TePla, GIGAbatch) with a power of 200 W for 1 min.

Simulations. The calculations are performed with the finite element method in the frequency domain by the commercial COMSOL Multiphysics software. Au nanorods are placed on the surface of ITO. The STM electrons are presented by a unitary harmonic point dipole source which is placed 1 nm above the sample surface. The tungsten tip is perpendicularly positioned 2 nm above the sample surface. The orientation of the point source is aligned along the axis of the tip. Unless stated otherwise, the STM tip is always included in the simulation. The STM-LE spectra are calculated by integrating the Poynting vector in the far field over a half sphere above the substrate. The probability of the IET process is proportional to the difference between the energy of the electron on the tip and the emitted photon.^{35,36} All simulated spectra are multiplied with a factor ($eV_{bias} - h\nu$).^{25,28} The radiative EM-LDOS (see Figure S4) is calculated by integrating the far-field Poynting vector over a full sphere covering the nanorods in vacuum.

The Au nanorods placed on ITO have lengths in the range of 55–155 nm, with a fixed diameter of ~11 nm. The refractive index of Au is adopted from Johnson et al.⁴⁴ The refractive index of ITO (thickness 150 nm) follows Moerland et al.⁵¹ The glass substrate is represented as a half-spherical space underneath the ITO, with a constant refractive index of 2.²⁵ Above the ITO is a vacuum space. A tungsten tip is modeled as a tip with an apex radius of 20 nm, a length of 400 nm, an opening angle of 12°, and a refractive index as adopted from Rakić et al.³³ Tungsten tips with different radii and opening angles are compared (see Figure S2). In the case of Figures 3 and 5, the tip apex radius is 100 nm to obtain an environment closer to the experiments. The whole system (nanorods and environments) is modeled in a sphere (thickness: 750 nm) surrounded by a perfectly matched layer (thickness: 150 nm). The discretization meshes range from 4 to 80 nm. Finer element size is used in meshing the nanorods to permit the study of the longitudinal plasmon modes.

STM-LE Setup. A custom-built STM instrument is operated in high vacuum (10^{-7} mbar) at room temperature. All measurements are performed with tungsten tips made by electrochemical etching in NaOH solution, giving tip radii of 30–100 nm. First, the emitted light is collected by a lens (Thorlabs, A110-B) with a numerical aperture of 0.4, placed at an incident angle of 60° from the sample normal. Then, the collected light is coupled to an optical fiber (Schaeffter + Kirchhoff, V-KF40-2x-MMC VIS/NIR-105-

NA022), which guides light through the vacuum chamber to the detector. The spectral information is acquired by a spectrograph (Princeton Instrument, SP2156i, 150 lines/mm grating) with a TE-cooled EMCCD (Andor, Newton 970P). STM-LE spectra are acquired at constant tunneling currents with feedback controls. All spectra are corrected by the relative detection efficiency in the wavelength range of 200–1000 nm, where the maximal detection efficiency is set to 1. The used STM-LE parameters are tip bias voltage, tunneling current, and integration time of the spectra.

ASSOCIATED CONTENT

Supporting Information

The Supporting Information is available free of charge at <https://pubs.acs.org/doi/10.1021/acsphtronics.2c01899>.

Simulated spectra with different tip sizes and tip positions and simulated radiative EM-LDOS (PDF)

AUTHOR INFORMATION

Corresponding Authors

Yalan Ma — Nanotechnology Group, ETH Zürich, CH-8803 Rüschlikon, Switzerland;  orcid.org/0000-0002-4772-7042; Email: mayala@ethz.ch

Andreas Stemmer — Nanotechnology Group, ETH Zürich, CH-8803 Rüschlikon, Switzerland; Email: astemmer@ethz.ch

Author

Olivier J. F. Martin — Nanophotonics and Metrology Laboratory, Swiss Federal Institute of Technology Lausanne (EPFL), CH-1015 Lausanne, Switzerland;  orcid.org/0000-0002-9574-3119

Complete contact information is available at: <https://pubs.acs.org/10.1021/acsphtronics.2c01899>

Notes

The authors declare no competing financial interest.

ACKNOWLEDGMENTS

The authors thank Blerim Veselaj (Nanotechnology Group, ETH Zürich) for technical support.

REFERENCES

- (1) Vahala, K. J. Optical microcavities. *Nature* **2003**, *424*, 839–846.
- (2) Novotny, L.; Hecht, B. *Principles of Nano-Optics*; Cambridge University Press, 2012.
- (3) Carminati, R.; Cazé, A.; Cao, D.; Peragut, F.; Krachmalnicoff, V.; Pierrat, R.; De Wilde, Y. Electromagnetic density of states in complex plasmonic systems. *Surf. Sci. Rep.* **2015**, *70*, 1–41.
- (4) Callahan, D. M.; Munday, J. N.; Atwater, H. A. Solar cell light trapping beyond the ray optic limit. *Nano Lett.* **2012**, *12*, 214–218.
- (5) Kelzenberg, M. D.; Boettcher, S. W.; Petykiewicz, J. A.; Turner-Evans, D. B.; Putnam, M. C.; Warren, E. L.; Spurgeon, J. M.; Briggs, R. M.; Lewis, N. S.; Atwater, H. A. Enhanced absorption and carrier collection in Si wire arrays for photovoltaic applications. *Nat. Mater.* **2010**, *9*, 239–244.
- (6) Knight, M. W.; Sobhani, H.; Nordlander, P.; Halas, N. J. Photodetection with active optical antennas. *Science* **2011**, *332*, 702–704.
- (7) Tang, L.; Kocabas, S. E.; Latif, S.; Okyay, A. K.; Ly-Gagnon, D.-S.; Saraswat, K. C.; Miller, D. A. Nanometre-scale germanium photodetector enhanced by a near-infrared dipole antenna. *Nat. Photonics* **2008**, *2*, 226–229.

- (8) Hoang, T. B.; Akselrod, G. M.; Argyropoulos, C.; Huang, J.; Smith, D. R.; Mikkelsen, M. H. Ultrafast spontaneous emission source using plasmonic nanoantennas. *Nat. Commun.* **2015**, *6*, No. 7788.
- (9) Kinkhabwala, A.; Yu, Z.; Fan, S.; Avlasevich, Y.; Müllen, K.; Moerner, W. E. Large single-molecule fluorescence enhancements produced by a bowtie nanoantenna. *Nat. Photonics* **2009**, *3*, 654–657.
- (10) Farahani, J. N.; Pohl, D. W.; Eisler, H.-J.; Hecht, B. Single quantum dot coupled to a scanning optical antenna: a tunable superemitter. *Phys. Rev. Lett.* **2005**, *95*, No. 017402.
- (11) Colas des Francs, G.; Girard, C.; Weeber, J.-C.; Dereux, A. Relationship between scanning near-field optical images and local density of photonic states. *Chem. Phys. Lett.* **2001**, *345*, 512–516.
- (12) Vignolini, S.; Intonti, F.; Riboli, F.; Wiersma, D. S.; Balet, L.; Li, L. H.; Francardi, M.; Gerardino, A.; Fiore, A.; Gurioli, M. Polarization-sensitive near-field investigation of photonic crystal microcavities. *Appl. Phys. Lett.* **2009**, *94*, No. 163102.
- (13) Verellen, N.; López-Tejeira, F.; Paniagua-Domínguez, R.; Vercruyse, D.; Denkova, D.; Lagae, L.; Van Dorpe, P.; Moshchalkov, V. V.; Sánchez-Gil, J. A. Mode parity-controlled Fano-and Lorentz-like line shapes arising in plasmonic nanorods. *Nano Lett.* **2014**, *14*, 2322–2329.
- (14) Zhang, S.; Chen, L.; Huang, Y.; Xu, H. Reduced linewidth multipolar plasmon resonances in metal nanorods and related applications. *Nanoscale* **2013**, *5*, 6985–6991.
- (15) Myroshnychenko, V.; Nelayah, J.; Adamo, G.; Gequet, N.; Rodríguez-Fernandez, J.; Pastoriza-Santos, I.; MacDonald, K. F.; Henrad, L.; Liz-Marzan, L. M.; Zheludev, N. I.; et al. Plasmon spectroscopy and imaging of individual gold nanodecahedra: a combined optical microscopy, cathodoluminescence, and electron energy-loss spectroscopy study. *Nano Lett.* **2012**, *12*, 4172–4180.
- (16) Rossouw, D.; Couillard, M.; Vickery, J.; Kumacheva, E.; Botton, G. Multipolar plasmonic resonances in silver nanowire antennas imaged with a subnanometer electron probe. *Nano Lett.* **2011**, *11*, 1499–1504.
- (17) Losquin, A.; Kociak, M. Link between cathodoluminescence and electron energy loss spectroscopy and the radiative and full electromagnetic local density of states. *ACS Photonics* **2015**, *2*, 1619–1627.
- (18) Arbouet, A.; Mlayah, A.; Girard, C.; Des Francs, G. C. Electron energy losses and cathodoluminescence from complex plasmonic nanostructures: spectra, maps and radiation patterns from a generalized field propagator. *New J. Phys.* **2014**, *16*, No. 113012.
- (19) Collins, S. M.; Nicoletti, O.; Rossouw, D.; Ostasevicius, T.; Midgley, P. A. Excitation dependent Fano-like interference effects in plasmonic silver nanorods. *Phys. Rev. B* **2014**, *90*, No. 155419.
- (20) Vesseur, E. J. R.; de Waele, R.; Kuttge, M.; Polman, A. Direct observation of plasmonic modes in Au nanowires using high-resolution cathodoluminescence spectroscopy. *Nano Lett.* **2007**, *7*, 2843–2846.
- (21) Kuttge, M.; Vesseur, E. J. R.; Koenderink, A. F.; Lezec, H. J.; Atwater, H. A.; de Abajo, F. G.; Polman, A. Local density of states, spectrum, and far-field interference of surface plasmon polaritons probed by cathodoluminescence. *Phys. Rev. B* **2009**, *79*, No. 113405.
- (22) Sapienza, R.; Coenen, T.; Renger, J.; Kuttge, M.; van Hulst, N. F.; Polman, A. Deep-subwavelength imaging of the modal dispersion of light. *Nat. Mater.* **2012**, *11*, 781–787.
- (23) Knight, M. W.; Liu, L.; Wang, Y.; Brown, L.; Mukherjee, S.; King, N. S.; Everitt, H. O.; Nordlander, P.; Halas, N. J. Aluminum plasmonic nanoantennas. *Nano Lett.* **2012**, *12*, 6000–6004.
- (24) Myrach, P.; Nilius, N.; Freund, H. J. Photon mapping of individual Ag particles on MgO/Mo (001). *Phys. Rev. B* **2011**, *83*, No. 035416.
- (25) Cao, S.; Zapata-Herrera, M.; Campos, A.; Le Moal, E.; Marguet, S.; Dujardin, G.; Kociak, M.; Aizpurua, J.; Borisov, A. G.; Boer-Duchemin, E. Probing the radiative electromagnetic local density of states in nanostructures with a scanning tunneling microscope. *ACS Photonics* **2020**, *7*, 1280–1289.
- (26) Le Moal, E.; Marguet, S.; Cannesson, D.; Rogez, B.; Boer-Duchemin, E.; Dujardin, G.; Teperik, T. V.; Marinica, D.-C.; Borisov, A. G. Engineering the emission of light from a scanning tunneling microscope using the plasmonic modes of a nanoparticle. *Phys. Rev. B* **2016**, *93*, No. 035418.
- (27) Parzefall, M.; Novotny, L. Optical antennas driven by quantum tunneling: a key issues review. *Rep. Prog. Phys.* **2019**, *82*, No. 112401.
- (28) Martín-Jiménez, A.; Fernández-Domínguez, A. I.; Lauwaet, K.; Granados, D.; Miranda, R.; García-Vidal, F. J.; Otero, R. Unveiling the radiative local density of optical states of a plasmonic nanocavity by STM. *Nat. Commun.* **2020**, *11*, No. 1021.
- (29) Schefold, J.; Meuret, S.; Schilder, N.; Coenen, T.; Agrawal, H.; Garnett, E. C.; Polman, A. Spatial resolution of coherent cathodoluminescence super-resolution microscopy. *ACS Photonics* **2019**, *6*, 1067–1072.
- (30) Kuhnke, K.; Grosse, C.; Merino, P.; Kern, K. Atomic-scale imaging and spectroscopy of electroluminescence at molecular interfaces. *Chem. Rev.* **2017**, *117*, 5174–5222.
- (31) Miroshnichenko, A. E.; Flach, S.; Kivshar, Y. S. Fano resonances in nanoscale structures. *Rev. Mod. Phys.* **2010**, *82*, 2257.
- (32) Douillard, L.; Charra, F.; Korczak, Z.; Bachelot, R.; Kostcheev, S.; Lerondel, G.; Adam, P.-M.; Royer, P. Short range plasmon resonators probed by photoemission electron microscopy. *Nano Lett.* **2008**, *8*, 935–940.
- (33) Rakić, A. D.; Djurišić, A. B.; Elazar, J. M.; Majewski, M. L. Optical properties of metallic films for vertical-cavity optoelectronic devices. *Appl. Opt.* **1998**, *37*, 5271–5283.
- (34) Dorfmüller, J.; Vogelgesang, R.; Weitz, R. T.; Rockstuhl, C.; Etrich, C.; Pertsch, T.; Lederer, F.; Kern, K. Fabry-Pérot resonances in one-dimensional plasmonic nanostructures. *Nano Lett.* **2009**, *9*, 2372–2377.
- (35) Persson, B. N. J.; Baratoff, A. Theory of photon emission in electron tunneling to metallic particles. *Phys. Rev. Lett.* **1992**, *68*, 3224.
- (36) Lambe, J.; McCarthy, S. Light emission from inelastic electron tunneling. *Phys. Rev. Lett.* **1976**, *37*, 923.
- (37) Le Moal, E.; Marguet, S.; Rogez, B.; Mukherjee, S.; Dos Santos, P.; Boer-Duchemin, E.; Comtet, G.; Dujardin, G. An electrically excited nanoscale light source with active angular control of the emitted light. *Nano Lett.* **2013**, *13*, 4198–4205.
- (38) López-Tejeira, F.; Paniagua-Domínguez, R.; Rodríguez-Oliveros, R.; Sánchez-Gil, J. A. Fano-like interference of plasmon resonances at a single rod-shaped nanoantenna. *New J. Phys.* **2012**, *14*, No. 023035.
- (39) Zhang, S.; Bao, K.; Halas, N. J.; Xu, H.; Nordlander, P. Substrate-induced Fano resonances of a plasmonic nanocube: a route to increased-sensitivity localized surface plasmon resonance sensors revealed. *Nano Lett.* **2011**, *11*, 1657–1663.
- (40) Chen, H.; Shao, L.; Ming, T.; Woo, K. C.; Man, Y. C.; Wang, J.; Lin, H.-Q. Observation of the Fano resonance in gold nanorods supported on high-dielectric-constant substrates. *ACS Nano* **2011**, *5*, 6754–6763.
- (41) Mayer, K. M.; Hafner, J. H. Localized surface plasmon resonance sensors. *Chem. Rev.* **2011**, *111*, 3828–3857.
- (42) Guo, L.; Jackman, J. A.; Yang, H.-H.; Chen, P.; Cho, N.-J.; Kim, D.-H. Strategies for enhancing the sensitivity of plasmonic nanosensors. *Nano Today* **2015**, *10*, 213–239.
- (43) Novotny, L. Effective wavelength scaling for optical antennas. *Phys. Rev. Lett.* **2007**, *98*, No. 266802.
- (44) Johnson, P. B.; Christy, R.-W. Optical constants of the noble metals. *Phys. Rev. B* **1972**, *6*, 4370.
- (45) Fung, E.-D.; Venkataraman, L. Too Cool for Blackbody Radiation: Overbias Photon Emission in Ambient STM Due to Multielectron Processes. *Nano Lett.* **2020**, *20*, 8912–8918.
- (46) Schull, G.; Néel, N.; Johansson, P.; Berndt, R. Electron-plasmon and electron-electron interactions at a single atom contact. *Phys. Rev. Lett.* **2009**, *102*, No. 057401.
- (47) Martin, J.; Kociak, M.; Mahfoud, Z.; Proust, J.; Gérard, D.; Plain, J. High-resolution imaging and spectroscopy of multipolar plasmonic resonances in aluminum nanoantennas. *Nano Lett.* **2014**, *14*, 5517–5523.

- (48) Li, S.; Miao, P.; Zhang, Y.; Wu, J.; Zhang, B.; Du, Y.; Han, X.; Sun, J.; Xu, P. Recent advances in plasmonic nanostructures for enhanced photocatalysis and electrocatalysis. *Adv. Mater.* **2021**, *33*, No. 2000086.
- (49) Badshah, M. A.; Koh, N. Y.; Zia, A. W.; Abbas, N.; Zahra, Z.; Saleem, M. W. Recent developments in plasmonic nanostructures for metal enhanced fluorescence-based biosensing. *Nanomaterials* **2020**, *10*, 1749.
- (50) Kumar, A. K. S.; Zhang, Y.; Li, D.; Compton, R.G. A mini-review: How reliable is the drop casting technique? *Electrochem. Commun.* **2020**, *121*, No. 106867.
- (51) Moerland, R. J.; Hoogenboom, J. P. Subnanometer-accuracy optical distance ruler based on fluorescence quenching by transparent conductors. *Optica* **2016**, *3*, 112–117.

□ Recommended by ACS

Broadband Enhancement of Optical Nonlinearity in a Plasmonic Nanocavity Coupled with an Epsilon-Near-Zero Film

Feilian Zhang, Yihang Chen, *et al.*

FEBRUARY 08, 2023

THE JOURNAL OF PHYSICAL CHEMISTRY C

READ ▶

Observation of Ultrabroadband Striped Space-Time Surface Plasmon Polaritons

Naoki Ichiji, Atsushi Kubo, *et al.*

JANUARY 11, 2023

ACS PHOTONICS

READ ▶

Exploiting Oriented Field Projectors to Open Topological Gaps in Plasmonic Nanoparticle Arrays

Álvaro Buendía, Vincenzo Giannini, *et al.*

JANUARY 11, 2023

ACS PHOTONICS

READ ▶

Finite-Element Method Simulations of the Tunable Magnetic Anapole State in an All-Graphene Metasurface: Implications for Near-Field Sensing, Nanoscale Optical Trapping, and...

Shuvajit Roy and Kapil Debnath

FEBRUARY 13, 2023

ACS APPLIED NANO MATERIALS

READ ▶

[Get More Suggestions >](#)